Ballistic dispersive shock waves in optical fibers

J. NUÑO[1,2], C. FINOT[1], G. XU[1], G. MILLOT[1], M. ERKINTALO[3,4], AND J. FATOME[1,*]

[1]*Laboratoire Interdisciplinaire Carnot de Bourgogne, UMR 6303 CNRS - Université Bourgogne-Franche-Comté, 9 av. A. Savary, Dijon, France*

[2] *Now at Departamento de Electrónica, Universidad de Alcalá, 28805 Alcalá de Henares (Madrid), Spain*

[3]*The Dodd-Walls Centre for Photonic and Quantum Technologies, New Zealand*

[4]*Department of Physics, The University of Auckland, Auckland 1010, New Zealand*

**Corresponding author: julien.fatome@u-bourgogne.fr*

We report on the first experimental and numerical observations of ballistic dispersive shock waves in optical fibers. In analogy with a supersonic object propagating through an inviscid perfect fluid, the vectorial shock waves are triggered by a double piston shock imprinted on a continuous-wave probe by a strong nonlinear cross-phase modulation produced by an orthogonally-polarized high-power pump pulse. The nonlinear phase profile imparted on the probe results in the formation of two oscillating fronts moving away from each other with opposite velocities, giving rise to an expanding zone of zero intensity. We show that the nonlinear dynamics at play can be described in terms of the interplay between wave-breaking and dispersive mapping, and we also investigate the impact of a group-velocity mismatch between the two interacting waves. Our experimental observations are in very good agreement with theoretical and numerical predictions derived from the celebrated Manakov model.

I. INTRODUCTION

The formation of dispersive shock waves (DSWs) is a fundamental mechanism encountered in many fields of science, such as hydrodynamics, geophysics, atmospheric science, socioeconomics, chemistry, acoustics, quantum fluids, and nonlinear optics [1-25]. One of the most fascinating manifestations of DSWs in nature is the appearance of the popular mascaret wave, which can be generated in specific river estuaries due to a counter-flow between tide and current, resulting in the formation of large undular tidal bores travelling up-stream; this phenomenon is particularly well-appreciated by the surfing community [1, 2]. Another spectacular manifestation of DSWs in atmospheric air-flow is the emergence of Morning Glory roll clouds and mountain waves [3]. In general, DSW phenomena occur in conservative (or weakly dissipative) non-viscous systems, and they rely on two fundamental ingredients: nonlinearity and wave dispersion. The most common situation involves the dispersive regularization of a jump gradient catastrophe – an example of the so-called Riemann problem – and gives rise to the expansion of non-stationary oscillating fan structures connecting both upper and lower initial non-oscillating states [5, 6]. Because of their universal role in counteracting unphysical singularities in dispersive conservative media, DSW prototypes have become the subject of intense research in physics, with groundbreaking experiments realized in diverse areas ranging from fluid dynamics to Bose-Einstein condensates [6-10, 22-25].

DSWs have also been observed and extensively studied in the context of nonlinear optics [9-21]. In particular, it is well-known that light behaves as an ideal inviscid perfect fluid in an optical medium that exhibits a weakly self-defocusing Kerr nonlinearity [10, 17-20]. Accordingly, the propagation of light through such a medium can be modeled using shallow water wave Euler equations, which predict that any initial

modulations experience a strong steepening that leads to the formation of a gradient catastrophe and subsequently DSWs [6, 18-20, 26]. This analogy has attracted significant attention, as it highlights the elegant prospect of using nonlinear optical systems as convenient laboratory testbeds for the exploration of universal DSW physics.

Ever since the pioneering work by Rothenberg and co-workers in optical fibers about two decades ago [9], tremendous efforts have been dedicated to develop powerful testbed platforms, which are capable of mimicking fluid-type DSWs with nonlinear optics [10-17]. Unfortunately, despite extensive attempts, the experimental generation and characterization of pure optical DSW remain challenging. In the vast majority of previous works, the DSWs are generated through the nonlinear steepening of an intense bright pulse superimposed on a continuous-wave background (CW) propagating in a self-defocusing nonlinear Kerr medium [16, 21]. Due to self-phase modulation, the high-intensity gradient region of the pulse generates new frequencies, which then disperse onto the plane-wave background creating an interference pattern that triggers the formation of DSWs [10, 16]. Although such experimental configurations have enabled valuable insights into DSW dynamics, they share a common deficiency: the CW landscape and the intense pump share a common optical mode. Because of this issue, a significant part of the physical information encoded on the CW landscape is hidden by the intense pump pulse itself, preventing its examination. Moreover, neither ballistic shock waves (sudden disturbances created by an external object propagating without dissipation or scattering), nor blast-wave, piston, and collision problems can be emulated [27-31]. To overcome these issues, one has to dissociate the DSW formation from the initial high intensity pump in such a way as to imprint the dispersive hydrodynamics phenomenon only on the CW landscape. An easy-to-implement laboratory platform capable of such dissociation would dramatically expand the DSW phenomena that can be investigated, enabling for instance the full emulation of a supersonic object (in the sense that it travels faster than the "speed of sound" within the medium), moving in a purely dispersive fluid [10, 27, 32].

Here we propose and experimentally demonstrate a novel nonlinear optical scheme that allows for the full isolation of DSW dynamics. Schematically illustrated in Fig. 1, our approach leverages the two orthogonal polarizations supported by silica glass optical fibers: an intense pump pulse acts as a piston that imprints a nonlinear phase shift through cross-phase-modulation (XPM) on an orthogonally polarized CW probe that is co-propagating in a normally dispersive optical fiber, resulting in the generation of two DSWs that are moving away from each other. More specifically, thanks to the orthogonal polarizations of the CW landscape and the intense piston pulse, the DSW dynamics can be straightforwardly isolated, permitting the first experimental observations of a depletion zone induced by two repulsive piston shock phenomena. To the best of our knowledge, our results represent the first experimental observations of vectorial DSWs generated in optical fibers, and more generally, the first observation of ballistic shock waves in nonlinear optics. We have also investigated how group-velocity mismatch between the CW landscape and the piston pulse impacts the DSW dynamics. Our work provides significant insights on the mechanism for the generation of DSWs and demonstrates a convenient platform that allows for the systematic and detailed experimental study of DSW physics.

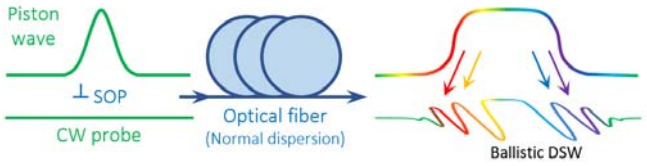

Figure 1. Principle. Schematic of the ballistic dispersive shock wave phenomenon.

II. MODELING AND PRINCIPLE OF OPERATION

Modeling

The system under study exploits the vectorial XPM interaction between a weak CW probe and an orthogonally polarized intense short pulse, both of which propagate in a normally dispersive optical fiber. In the framework of nonlinear fiber optics [33], the evolution of the complex slowly varying amplitudes of the pump pulse $u(z,t)$ and the CW probe $v(z,t)$ are described by a set of two coupled nonlinear Schrödinger (NLS) equations. In standard optical fibers, random longitudinal fluctuations of the residual birefringence occur along the fiber in a length-scale of a few meters. Averaging out the nonlinear contribution over these fast polarization fluctuations in km-long fibers leads to the so-called Manakov model [34, 35]:

$$\begin{cases} i\dfrac{\partial u}{\partial z}+\dfrac{\beta_2}{2}\dfrac{\partial^2 u}{\partial t^2}+\dfrac{8}{9}\gamma\left(|u|^2+|v|^2\right)u+i\dfrac{\alpha}{2}u=0, \\ i\dfrac{\partial v}{\partial z}+i\delta\dfrac{\partial v}{\partial t}+\dfrac{\beta_2}{2}\dfrac{\partial^2 v}{\partial t^2}+\dfrac{8}{9}\gamma\left(|u|^2+|v|^2\right)v+i\dfrac{\alpha}{2}v=0 \end{cases} \quad (1)$$

Here, z and t denote the propagation distance coordinate and time in the co-moving frame of the piston pump pulse, respectively. γcorresponds to the nonlinear Kerr parameter of the fiber, β_2 is the group velocity dispersion coefficient, and α indicates propagation losses. The corrective factor of 8/9 is applied to the Kerr effect due to the polarization randomness

assumed in the Manakov model. The term $\delta = 2\pi\beta_2\,\delta f$ describes the walk-off between the pulse and the CW landscape when the central frequencies of the two are separated by a small frequency offset δf. Let us stress that no transfer of energy occurs between the two waves during the nonlinear interaction. Indeed, it should be clear from Eqs. (1) that the two waves are only coupled by a phase term, which is proportional to the intensity of the waves. Accordingly, the energy initially contained in the CW probe (or piston pulse) remains unchanged (except for linear losses). Note that we neglect higher-order effects such as third-order dispersion, self-steepening and Raman scattering, as they have been found to play a negligible role in the present dynamics. This assumption is verified *a posteriori* by the excellent agreement between our experimental observations and numerical modeling.

In terms of fluid-like or condensate variables, the set of coupled NLS equations above can be cast into their hydrodynamic forms by means of the well-known Madelung transformation [6, 8, 10, 17] (see Appendix A). In this configuration, the intensity and the gradient of the phase (chirp profile) assume respectively the roles of the density and velocity of the fluid. It then turns out that the exchange of momentum during the shock process is here induced by the XPM coupling term which acts as a sharp defocusing potential for the fluid. In a sense, our experiment constitutes the 1-D counterpart of the blast-wave or *double* piston shock problem already studied in quantum superfluid and induced by a laser beam [8, 10, 28, 29]. The background density which sets the reference speed of sound is here dictated by the intensity level of the CW landscape, while strong density perturbations (here the high-power pump beam) naturally correspond to supersonic sources [10, 22].

Dynamics of the dispersive ballistic shock wave

We begin by numerically illustrating the formation and evolution of ballistic DSWs in a vectorial configuration. To this end, we consider the following set of parameters which mimics the experiments that will follow. The piston pump wave is a Gaussian-like chirp-free pulse with the following characteristics: temporal half-width at *1/e* of its maximum intensity t_0 = 41 ps, peak power P_c = 1.5 W and central wavelength λ_p= 1550 nm. The orthogonally polarized CW probe propagates with the same group velocity as the piston beam (δf=0) and its average power is set to be 10 mW. The normally dispersive fiber is a 13-km-long dispersion compensating fiber (DCF) typically used in the field of dispersion managed data transmission (for parameters, see Appendix B). It is important to emphasize that the above physical parameters place our problem in the weakly dispersive regime of the NLS (at least in the initial stage of propagation), for which the ratio between the nonlinear and dispersive effects – given by the usual soliton number N – is much larger than unity. Indeed, with the maximum pump power in our experiments, we have $N = \sqrt{L_d / L_{nl}} = \sqrt{\gamma'\, P_c\, t_0^2 / \beta_2} \approx 14$ [33], where $\gamma' = 8\,\gamma/9$. Accordingly, the analogy between nonlinear optics and shallow water hydrodynamics is fully appropriate for our study, at least in the early stage of propagation (see the Appendix A for further details on the analogy).

Figure 2 shows numerically simulated dynamics of ballistic DSW generation. Focusing first on the piston field $u(z,t)$ [Figs. 2(a) and (b)], we see dynamics typical for an intense pulse propagating in a defocusing Kerr medium [36, 37]. The initial stages of the evolution are dominated by self-phase-modulation, which gives rise to strong spectral broadening [cf. Fig. 2(a)]. This initial spectral broadening ceases at the so-called wave breaking distance z_c at which point the spectral width reaches the maximum value of Δf_{max}. Both z_c and Δf_{max} can be accurately estimated using theories of the ubiquitous wave-breaking phenomenon [36, 37]:

$$z_c \approx \frac{1.61\, t_0}{\sqrt{\beta_2\, \gamma'\, P_c}} \qquad \textbf{(2)}$$

$$\Delta f_{\max} = \frac{1}{2^{1/4}\,\pi}\sqrt{\frac{\gamma'\, P_c}{\beta_2}} = \frac{N}{2^{1/4}\,\pi\, t_0} \qquad \textbf{(3)}$$

As shown with the cyan dashed-line and open circles in Fig. 2(a), these estimates are in very good agreement with our simulations.

Following the initial stage of spectral broadening, chromatic dispersion dominates, resulting in strong temporal expansion [Fig. 2b]. In accordance with the principles of dispersive Fourier transform [38-40], the piston pulse spectrum maps into the temporal domain during propagation; in the far-field, both the spectral and temporal profiles of the pulse exhibit similar parabolic profiles [38, 41]. The maximal temporal width Δt_{max} of the piston pulse at position z can be estimated by:

$$\Delta t_{\max} = 2^{3/4}\, z\sqrt{\gamma'\, P_c\, \beta_2} \approx 2.71\, z / z_c \qquad \textbf{(4)}$$

As highlighted with the dashed white lines in Fig. 2(b), this expression agrees very well with the temporal expansion of the piston pulse observed in our numerical simulations.

Let us now consider the CW probe beam $v(z,t)$. In the initial stage of evolution (during which the piston pulse temporal profile stays almost constant), XPM coupling gives rise to a non-uniform nonlinear phase shift that increases linearly with propagation $\phi_{nl}(z,t) \approx \gamma' \left|u(0,t)\right|^2 z$ [42]. As evidenced by the strong spectral broadening of the probe beam [c.f. Fig. 2(c)],

this nonlinear phase shift gives rise to an instantaneous frequency shift (chirp) $\delta\omega(z,t) = -\partial_t \phi_{nl}(z,t) = -\gamma' z \partial_t |u(0,t)|^2 z$ across the CW landscape: the region overlapping with the leading (trailing) edge of the piston pulse is redshifted (blueshifted). Since blue light travels slower than red light in normally dispersive media, this chirp manifests itself in the temporal domain as an instantaneous change of velocity V around the central portion of the probe/piston pulse, with $\delta V(z,t) \propto -\beta_2 \delta\omega(z,t)$. We consequently observe the emergence of two fronts with opposite velocities that are travelling away from each other, as well as the concomitant removal of energy from the central region defined by the initial piston pulse [see Fig. 2(d)]. With subsequent propagation, chromatic dispersion begins to regulate the steep edges of the fronts, giving rise to the development of fast non-stationary oscillations surrounding a temporal gap – a characteristic imprint of a ballistic or double piston DSW [8, 28].

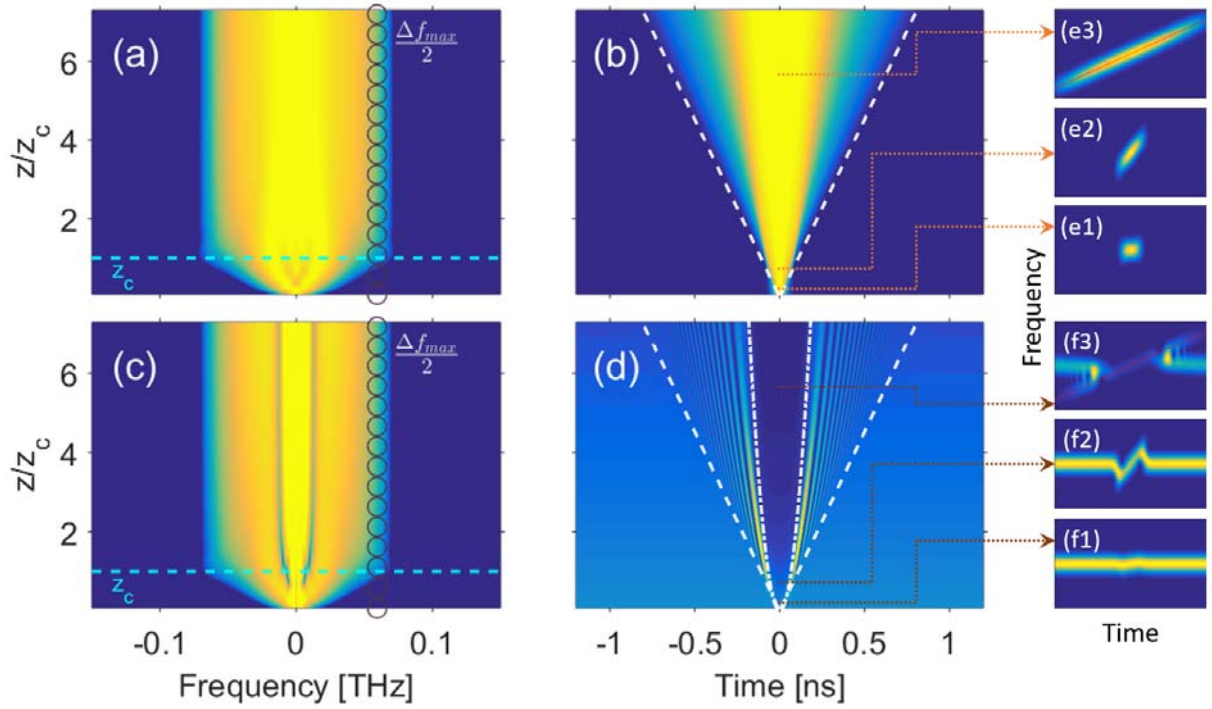

Figure 2. Illustrative numerical simulations. (a, c) Longitudinal evolution of the spectrum of the (a) piston pulse and (c) probe wave. The cyan dashed-line indicates the distance z_c predicted by Eq. (2), while the open circles highlight $\Delta f_{max}/2$ predicted by Eq. (3). **(b, d)** Longitudinal evolution of the temporal intensity profiles of the (b) piston pulse and (d) probe wave. Analytical predictions of the temporal expansion provided by Eqs. (4) and (5) are plotted using white dashed- and dash dotted-line, respectively. The simulation results were obtained using parameters corresponding to our experiments (see Appendix B) and for a pulse peak power of 1.5 W. **(e_1-e_3)** Spectrograms of the piston pulse at z = 0.05, 0.7 and 5.6 z_c, respectively. **(f_1-f_3)** Corresponding spectrograms of the probe wave. The spectrograms are plotted on a linear scale and extend from -300 ps to 300 ps (horizontal axis) and from -80 GHz to 80 GHz (vertical axis). The red lines in panels (e_3) and (f_3) indicate the far field chirp profile of slope $1/(\beta_2 z)$.

The overall dynamics are very well captured when illustrating the evolution of the probe beam by means of a spectro-temporal approach [43, 44]. To this aim, we have displayed in panels (e_1-e_3) and (f_1-f_3), the spectrograms of the piston and probe waves at z = 0.05, 0.7 and 5.6 z_c, respectively. As can be observed, the piston pulse experiences a large temporal and spectral expansion, while the interplay between dispersion and nonlinearity subsequently induces, after the wave breaking distance z_c, a close-to-linear chirp with a slope given by $1/(\beta_2 z)$, indicated with red lines in panels (e_3 & f_3) [38]. The dynamics of the cw probe is markedly more complex than the dynamics of the pump. Because of the XPM coupling, the piston beam induces on the CW landscape a chirp profile proportional to the gradient of its intensity profile. Note in particular that, during the early stage of propagation (Fig. 2(f2) at $z = 0.7\, z_c$), a typical N-wave shape of the chirp profile forms through a process analogous to the formation of a pressure wave occurring during a supersonic boom event [27, 45]. Then, as the piston pulse expands and develops steeper and steeper edges, the redshifted and blueshifted parts of the probe are pushed away from the center due to chromatic dispersion, creating a temporal gap which continuously expands over propagation.

On both sides of this rarefaction area, a DSW emerges from the fast oscillations occurring between the remaining continuous wave background and new frequencies [16].

Because the nonlinear phase imparted on the probe beam is dominated by XPM, Eqs. (2-4) also apply when describing the temporal and spectral spreading of the DSW, as shown in Figs. 2(c) and (d). Here it is worth emphasizing that Eq. (4) in particular captures the universal fact that the rate of expansion of a DSWs is a square-root function of the medium density, portrayed in our optical system by the intensity jump [6, 8, 32]. Moreover, we note that, when plotted versus the normalized distance z/z_c, the shock cone imposed by the piston pulse is only determined by the sharpness of the source, i.e. t_0. That is to say, the angle of the white dashed-lines cone is simply provided by $tan^{-1}(2.71\, t_o)$.

By considering the peak power reduction of the piston pulse due to temporal broadening along the propagation distance and neglecting fiber losses, we can also derive an estimate for the rarefaction area $\Delta t_{\min}$ that describes the width of the temporal gap created within the probe landscape:

$$\Delta t_{\min} = 2^{3/4}\, z \sqrt{\gamma' P_{\min} \beta_2} \qquad \textbf{(5)}$$

where

$$P_{\min} = P_c \frac{t_0}{\Delta t_{\max}} \qquad \textbf{(6)}$$

As highlighted with the dash dotted white line in Fig. 2(d), this estimate of $\Delta t_{\min}$ agrees well with our simulation results and illustrates the fact that the rate of expansion of the rarefaction area is not constant but rather decelerates with propagation.

III. RESULTS

Experimental setup

To experimentally generate and observe ballistic DSWs, we have implemented the setup depicted in Fig. 3(a) [see Appendix B for additional details]. 68-ps Gaussian-like optical pulses are first generated by intensity modulating a 1550 nm CW laser. This pulse train is then amplified using an Erbium doped fiber amplifier (EDFA) and used as the piston pump wave. The probe wave consists of a 10-mW CW which can be generated at the same central wavelength as the piston pulse or at a distinct wavelength to explore the effect of a variable velocity mismatch between the piston and the probe signals. Both waves are then orthogonally polarized using a polarization beam splitter (PBS), and injected into a 13-km-long segment of normally dispersive compensating fiber (see Appendix B for detailed parameters). At the output of the system, the piston and the probe waves are polarization demultiplexed and subsequently characterized in the temporal and spectral domains. Note that this experimental testbed platform relies exclusively on commercial devices widely used in the telecommunication industry, and that the all-fibered nature of the setup ensures stable operation for several consecutive hours.

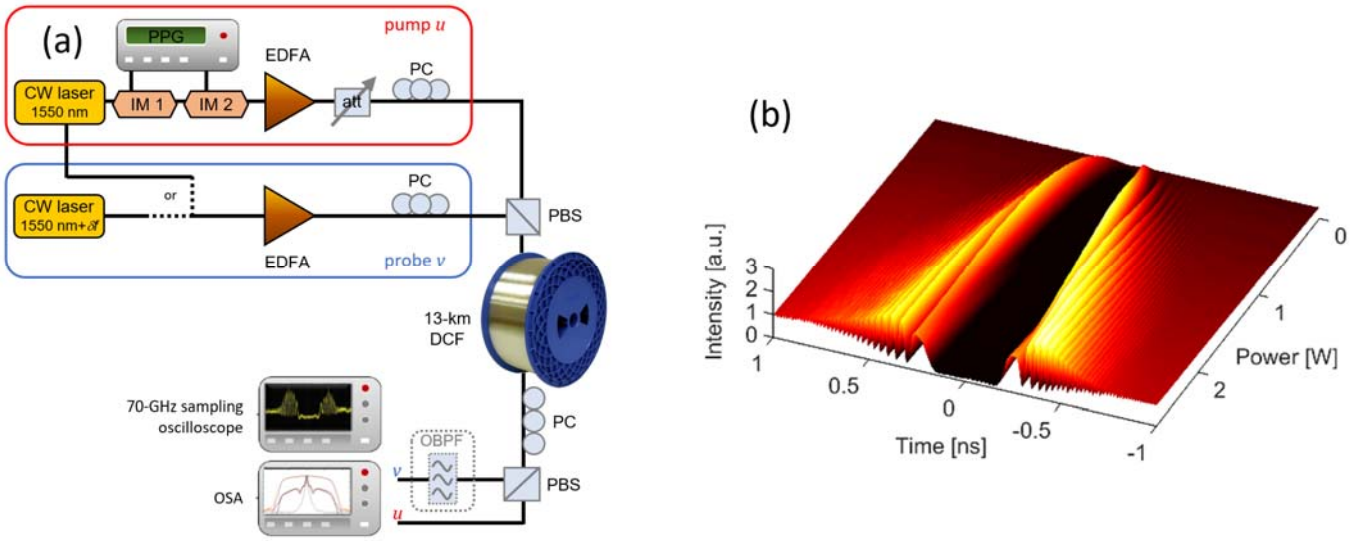

Figure 3. Experimental setup and illustrative observations of ballistic DSW dynamics. (a) Experimental setup: CW, Continuous Wave; PPG, Pulse Pattern Generator; IM, Intensity Modulator; EDFA, Erbium Doped Fiber Amplifier; Att, Optical Attenuator; PC, Polarization Controller; PBS, Polarization beam splitter; DCF, Dispersion Compensating Fiber; OBPF, Optical BandPass Filter; OSA, Optical Spectrum Analyzer. **(b)** False-color plot showing the experimentally recorded evolution of the output intensity profile of the probe beam as a function of the input piston pulse peak power. Data values are normalized with respect to the CW landscape equal to 1 and mapped to colors linearly.

Experimental observation of ballistic DSWs

Figure 3(b) shows experimentally measured DSW dynamics when a single CW laser is used for both the piston pulse and the probe wave (null walk-off configuration, δf=0). Specifically, here we depict the probe beam intensity profile recorded on our sampling oscilloscope for a range of piston powers. (Note that varying the piston peak power at constant fiber length yields similar insights as recording the longitudinal evolution of the fields at maximum power, but avoids the use of a destructive cutback method). In accordance with the qualitative description presented above, we see very clearly that the CW landscape of the probe beam is broken by two repulsive fronts imposed by the double piston effect. As the piston peak-power increases (and the shock becomes more abrupt), the oscillations in the tails of the fronts increase in frequency. This process is analogous to the 1-D behavior of blast DSWs created by a supersonic object (laser beam) propagating through a quantum fluid [8], with the defocusing potential imposed in our system by the pump-induced XPM. Our experimental observations are in quantitative agreement with theoretical predictions and numerical modelling, as shown in Fig. 4. Here we compare the experimentally measured intensity profiles of the probe [Fig. 4(a)] and piston [Fig. 4(b)] beams as a function of the piston pulse peak power with corresponding results from numerical simulations [Figs. 4(c) and (d)]. The agreement between our experiments and simulations is remarkable. We emphasize that no free-running fitting parameters were used: the simulations make exclusive use of experimental parameters. Moreover, as highlighted by the white dashed curves and dash-dotted lines in Fig. 4, we see how the experimentally-resolved dynamics of the DSW process (e.g. width of the gap region in the probe wave and the width of the piston pulse beam) agrees extremely well with the analytical predictions based on Eqs. (4) and (5).

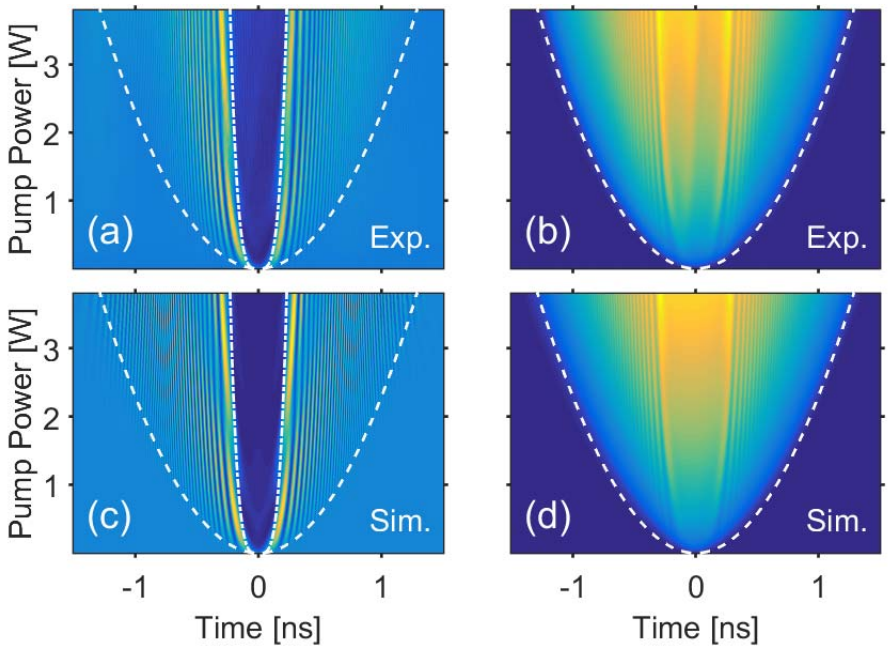

Figure 4. Comparison between experimental, theoretical, and numerical results. (a, b) Pseudo-color plots depicting the evolution of the output temporal intensity profile of the (a) probe wave and (b) the piston beam as a function of the injected piston peak-power. (c, d) Corresponding numerical simulation results. For the probe panels, data values are normalized by the level of the CW landscape, while the piston panels are normalized by the maximum available peak power. The white dashed lines and dash-dotted lines highlight theoretically predicted dynamics of the shock expansion based on Eqs. (4) and (5), respectively.

To gain further insights, Fig. 5 shows a comprehensive input-output analysis of the piston and probe waves for an injected pulse peak-power of 1.5 W. First, Fig. 5(a) compares the input and output intensity profiles of the piston pulse, revealing the large temporal broadening that takes place in the DCF: the half-width of the piston pulse increases from 68 ps (blue solid line) to more than 1.4 ns (yellow line). As highlighted by the open circles, we also see that the profile of the output pulse can be very well approximated with a parabolic profile of width Δt_{max} given by Eq. (4). However, small oscillations that deviate from the parabolic shape are visible on the edges of the pump profile. These oscillations originate from the back-action of the ballistic DSW on the piston pulse through XPM, as confirmed by the fact that no oscillation is observed when only the pulse propagates through the fiber (magenta solid curve). Figure 5(b) compares the input and output intensity profiles of the

probe wave. Here the dramatic transformation of the CW landscape into a ballistic DSW can be readily observed. Indeed, the output intensity profile is characterized by a wide-open temporal gap surrounded by two strongly modulated wave trains. We must emphasize that the oscillating fan structure of the fronts can be fully resolved in our system, underlining its potential to provide exquisitely detailed insights into DSW dynamics. Moreover, the absence of any major asymmetry, typically caused by e.g. third-order dispersion, self-steepening or Raman scattering, confirms the purity of the system. Indeed, the small amplitude asymmetry observed between the two DSW is attributed to the small asymmetry of the input pulse which can be mitigated by further optimization. It is interesting to note that the oscillations displayed by the DSWs are chirped, i.e., their period is changing, in agreement with classical regularization of DSW [6]. This feature is fully reproduced by our numerical simulations, as shown by the vertical dashed lines in Fig. 5(b), which highlight the positions of the oscillation maxima extracted from our simulations. As explained in the Appendix C [see Fig. 7], this feature can be readily explained in terms of the dispersion-induced spectro-temporal mapping of the DSW.

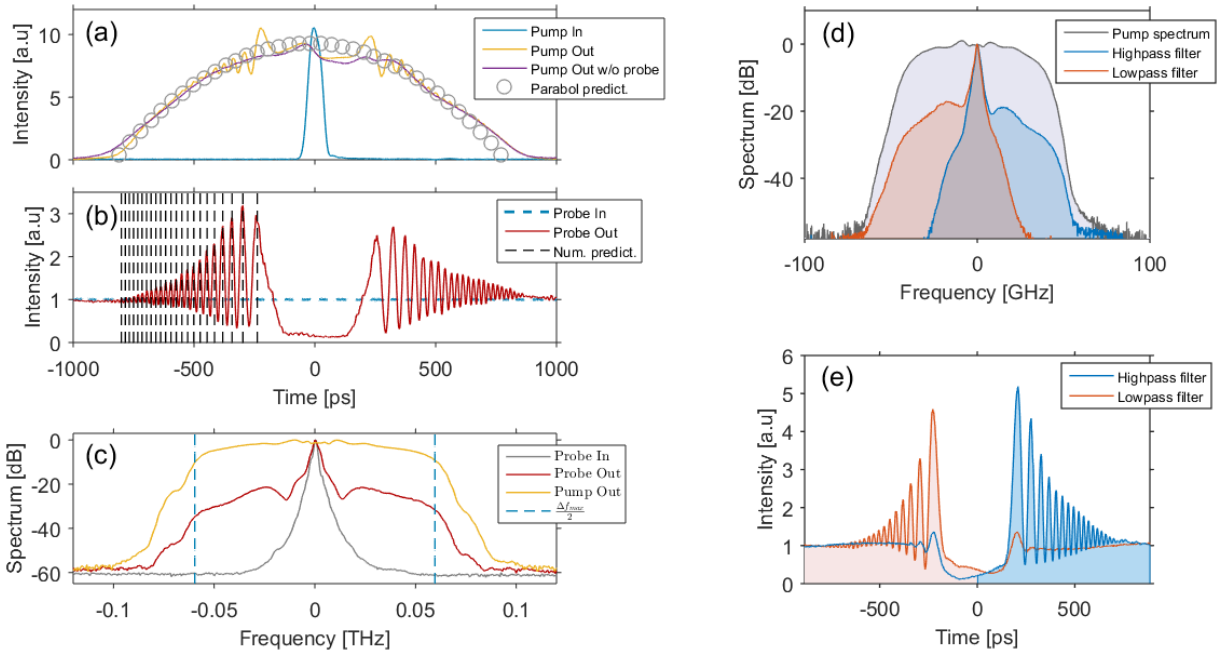

Figure 5. Input-output comparison of the piston pulse and probe wave for a peak power of 1.5 W. **(a)** Blue solid line shows the input temporal profile of the piston pulse, while the yellow and purple lines show the corresponding output profiles in the presence and absence of the CW probe, respectively. Open circles correspond to a parabolic profile of width Δt_{max}. **(b)** Temporal profile of the probe wave at the fiber input (blue dashed line) and output (red solid line). Vertical black dashed lines indicate the positions of the oscillation maxima predicted by numerical simulations based on Eqs. (1). Note that, in panel (b), data values are normalized with respect to the output cw landscape, while in panel (a) an arbitrary normalization is used for convenience and clarity. **(c)** Experimental spectra of the initial and output probe beam compared to the output piston spectrum. Theoretical prediction of the maximum spectral expansion Δf_{max} is also displayed with blue dashed lines. **(d-e) Spectro-temporal characterization of ballistic DSWs (d)** Experimental output spectrum after optical filtering obtained for a piston pulse peak power of 1 W. **(e)** Output temporal intensity profile of the probe signal after spectral filtering. Resulting profile in red (blue), when only the low (high) frequencies are conserved.

Figure 5(c) compares the input and output spectral profiles of the probe and piston pulse beams. As can be seen, both waves undergo significant spectral broadening, characterized by an output total spectral expansion above 150 GHz – a value very close to the theoretical prediction Δf_{max} (blue dashed lines). In this context, it is worth noting that the piston pump and the probe spectra exhibit very similar profiles, underlining the fact that XPM dominates the nonlinear evolution of the probe. We must also emphasize that, in accordance with the theoretical description presented above [see spectrograms in Fig. 2], the different spectral components of the probe beam are temporally segregated amongst the two DSWs, with redshifted (blueshifted) frequency components associated with the leading (trailing) edge of the DSW. We have experimentally confirmed this feature by recording the spectral and temporal intensity profiles of the probe beam after it has passed through a 1-nm optical bandpass filter off-set from the 1550 nm center

wavelength. Results are shown in Figs. 5(d) and (e), and they readily show that filtering induces a striking asymmetry in the temporal intensity profile. Indeed, by filtering the output spectrum of the probe, we are able to annihilate half of the shock. More precisely, after cancelling the higher frequencies (red curves), the temporal fan recorded for $t > 0$ vanishes. In contrast, when higher frequencies and the continuous component are preserved (blue curves), the leading fan disappears. In both cases, the central hole still occurs since no energy is present in this part of the shock

Influence of a velocity mismatch

Before concluding, we discuss the impact of relative walk-off between the probe and the piston beams. In this case, the ballistic shock is triggered by a pulse that is moving relative to the CW landscape (in analogy with a projectile impacting a displacing target), resulting in asymmetric DSW dynamics. To experimentally engineer such a scenario, we create the piston pulse and the probe beams using two separate lasers with an adjustable frequency offset δf. (This should be contrasted with the experiments reported in the preceding section that only used a single laser.) Thanks to group-velocity dispersion, the probe and the piston beams travel with slightly different (group) velocities through the fiber, while nonlinearly interacting through XPM. In Fig. 6(a), we show the temporal intensity profile of the probe beam at the fiber output, when the piston pulse peak power is set to 2 W and the frequency offset δf = 100 GHz (corresponding to a total walk-off of 1.29 ns over the 13-km-long fiber). We see clear signatures of asymmetric DSW dynamics, with an enhanced fan structure observed exclusively on the trailing part of the shock. By inverting the sign of the frequency offset (δf = -100 GHz), the asymmetry is correspondingly inverted, with a clear fan structure on the leading part of the shock [see Fig. 6(b)]. A more comprehensive picture of the effect of relative walk-off is provided in Fig. 6(c), where we show the probe beam intensity profile at the fiber output over a wide range of frequency offsets. Also shown as the dashed line is the trajectory of the piston pulse (i.e., the temporal position of the pump pulse center at the fiber output), which precisely follows the dispersive walk-off imposed by the frequency offset between the two waves. As expected, the shock waves vanish when the group-velocity difference between the two beams becomes larger than the expansion speed of the shock – dictated by the maximum frequency chirp (here around 70 GHz). These experimental results are again in excellent agreement with the corresponding numerical simulations, shown in Fig. 6(d).

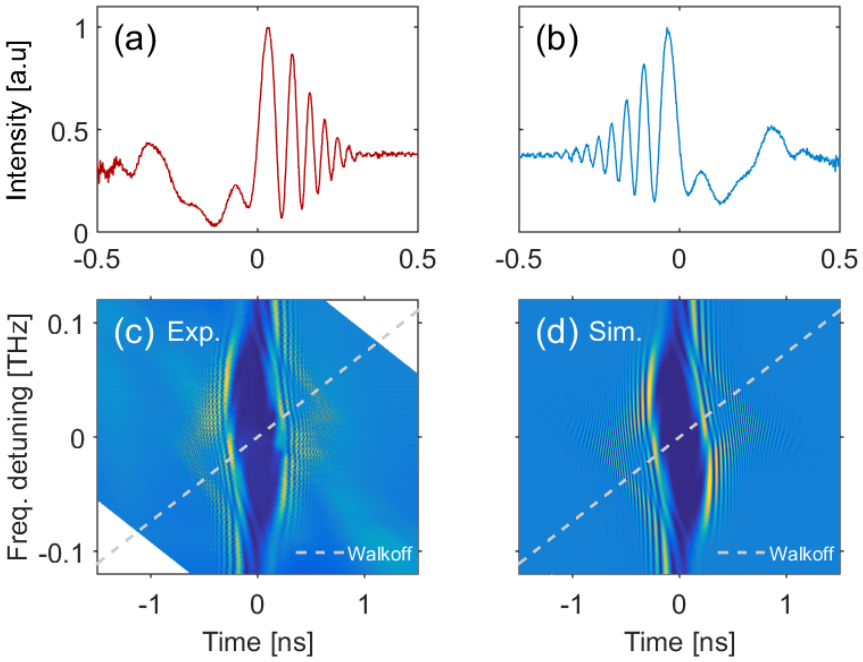

Figure 6. Influence of a velocity mismatch. (a, b) Temporal intensity profile of the probe beam at the fiber output for an offset frequency of (a) δf = 100 GHz and **(b)** δf = –100 GHz. **(c)** Experimentally measured output intensity profile of the probe wave as a function of frequency detuning δf. **(d)** Corresponding simulation results. Data in (c) and (d) are normalized by the level of the CW intensity landscape. The dashed line shows the relative position of the piston pulse center (initially at zero) at the fiber output.

IV. DISCUSSION AND CONCLUSIONS

In conclusion, we have reported on the first experimental demonstration of ballistic dispersive shock waves in the context of nonlinear fiber optics. Our scheme leverages the nonlinear XPM interaction between a weak CW probe co-propagating in a normally dispersive optical fiber and an orthogonally polarized intense piston pulse. In contrast to previous studies, which have exclusively operated in the scalar regime, our system enables the generation of DSWs in a two-component vectorial configuration. Because the generated DSW is orthogonally polarized with respect to the intense piston beam, it can be fully isolated and characterized without being obscured by the pump pulse. Using this scheme and the correspondence between nonlinear optics and non-viscous hydrodynamics, we have been able to realize an optical analog of a double piston DSWs induced by a supersonic object moving across a superfluid-like medium, as characterized by the appearance of two repulsive, rapidly oscillating fronts surrounding a region of zero intensity. All our experimental observations are in excellent agreement with numerical simulations of the celebrated Manakov model, and they adhere to simple analytical guidelines predicted from established theories of wave breaking and spectro-temporal mapping induced by chromatic dispersion.

We anticipate that the presented results will stimulate analytical and statistical research that is above the scope of the present paper. We have shown how the piston pulse drives the evolution towards the shock and continuously affects its evolution; future works may for example focus on how the use of a chirped piston pulse could be beneficial to control the longitudinal evolution of the probe wave and associated DSWs. More generally, shock wave phenomena are often difficult to study in their natural environment, and also hard to reproduce in laboratory. Therefore, we believe that the present numerical and experimental research fully demonstrates that fiber optics may constitute a remarkable testbed platform for the experimental characterization of DSWs. Moreover, in contrast to numerous other implementations, our fiber-based approach constitutes a new avenue to produce and study ballistic dispersive shock waves in a non-destructive manner, by means of a compact, highly stable and high reproducible system. We therefore expect that other fields of physics involving two component interactions may be inspired by this research [46].

Acknowledgment. JF acknowledges the financial support from the European Research Council (Grant Agreement 306633, PETAL project), the FEDER, the Conseil Régional de Bourgogne Franche-Comté (International Mobility Program) which has allowed him to visit The University of Auckland to contribute to this work. CF and GM acknowledge support from Institut Universitaire de France (IUF). We also thank EUR eiphy (ANR-17-EURE-0002), project ISITE-BFC (contract ANR-15-IDEX-0003). ME acknowledges support from the Rutherford Discovery Fellowships and Marsden Funds administered by the Royal Society of New Zealand. All the experiments were performed on the PICASSO platform in ICB. We also thank A. Picozzi, and D. Castelló-Lurbe for fruitful discussions.

APPENDIX A: Hydrodynamic modeling

Equations (1) of the main text can be further simplified via additional approximations in order to focus on the main physical insights of the problem and allow a convenient transformation of the Manakov model into a hydrodynamic form. As a first approximation, we may neglect fiber losses by setting $\alpha = 0$. We can also consider that the pump *u(z,t)* and the probe *v(z,t)* have identical central frequencies so that the walk-off parameter is null, $\delta = 0$. Moreover, as the initial peak-power of the pump pulse *u(z,t)* is much larger than the power of the probe *v(z,t)*, we can neglect the cross-phase modulation involved with the weaker probe on the pump signal. With these assumptions, Eqs. (1) can be cast into the following normalized form:

$$\begin{cases} i\varepsilon \dfrac{\partial u}{\partial Z} + \dfrac{\varepsilon^2}{2}\dfrac{\partial^2 u}{\partial T^2} + |u|^2 u = 0 \\ i\varepsilon \dfrac{\partial v}{\partial Z} + \dfrac{\varepsilon^2}{2}\dfrac{\partial^2 v}{\partial T^2} + (|v|^2 + |u|^2)v = 0 \end{cases} \quad \textbf{(7)}$$

Here the time and distance have been respectively normalized as $Z = z/\sqrt{(L_d L_{nl})}$, $T = t/t_0$, while *u(z,t)* and *v(z,t)* have been normalized by their respective (peak) power and $\varepsilon = 1/N$. In this work, $\varepsilon = 0.07$ at the maximum pump power reached in the experiment, implying that the present light-flow can be considered as a perfect fluid [6, 10, 17, 28].

Similarly to the case of the Gross-Pitaevskii equation describing Bose-Einstein condensates, the set of coupled nonlinear Schrödinger equations written above can be turned into "hydrodynamic form" by means of the well-known Madelung transformation [6, 17, 28]. More precisely, writing the pump and probe beams in polar form as $u(z,t) = \sqrt{\Gamma(t,z)}exp\big(i\phi(Z,T)\big)$ and $(z,t) = \sqrt{\rho(t,z)}exp\big(i\varphi(Z,T)\big)$,

respectively, and separating the real and imaginary parts, we obtain the following hydrodynamic-like conservation laws:

$$\begin{cases} \Gamma_Z + (\Gamma\,\varsigma)_T = 0 \\ \varsigma_Z + \left(\frac{1}{2}\varsigma^2 + \Gamma\right)_T = 0, \end{cases} \quad \textbf{(8)}$$

$$\begin{cases} \rho_Z + (\rho\,\mu)_T = 0 \\ \mu_Z + \left(\frac{1}{2}\mu^2 + \rho\right)_T = -\Gamma_T = -V(Z,T) \end{cases} \quad \textbf{(9)}$$

Here Γ and ρ denote the fluid densities associated with the pump and probe beams, respectively, while $\varsigma = \phi_T$ and $\mu = \varphi_T$ are the corresponding flow velocities. (Subscripts designate partial derivatives.) In analogy with the shock waves observed in Bose-Einstein condensates [6-10, 22-25], we can clearly see that the shock induced on the probe wave is triggered by the XPM potential source $V(Z,T) = \Gamma_T$, which plays the role of the double piston. The main difference with a classical piston shock problem is that this potential is neither constant in time nor in propagation distance, since the initial pulse follows the evolution of a Spectron [38, 47]. It is worth mentioning that the potential term $V(Z,T)$ in Eq. (9) decreases with propagation, which means that the action of the external piston on the probe wave is decelerating upon propagation. In this situation, the dynamics are more complex and cannot be considered as in Ref. [28] as a constant piston shock problem. For full quantitative description, more intensive research involving the celebrated Whitham modulation theory is still required but is far beyond the scope of this experimental paper.

APPENDIX B: Additional details on the experimental setup

Further details are given with reference to Fig. 3. The testbed platform involved in the observation of ballistic DSW is all-fibered and relies exclusively on commercial devices widely used in the telecommunication industry. First-of-all, a train of 68-ps pulses at a repetition rate of 312.5 MHz is generated at 1550 nm by means of a CW laser from Exfo modulated thanks to a 14-Gbit/s pulse-pattern generator (PPG form Anritsu Corporation). Two $LiNbO_3$ intensity modulators from Ixblue photonics (IM1 & IM2) are subsequently cascaded in order to improve the extinction-ratio (ER) of the generated piston pulses. In this way, an ER higher than 40 dB is achieved, thus preventing any spurious interference between the piston pulse and the residual background [16, 21]. This pulse train is then amplified by means of a 33-dBm Erbium doped fiber amplifier (EDFA from Manlight) and used as piston pump beam whose power can be continuously tuned thanks to a programmable variable optical attenuator (Exfo), thus ensuring an efficient stability of the setup, especially on polarization states. The probe wave consists of a 10-mW CW landscape which can be a simple replica of the initial 1550-nm signal to ensure a perfect velocity matching (null walk-off configuration, δ= 0 in Eqs. (1)) or a distinct CW generated from a second external cavity laser from Exfo so as to induce a variable velocity mismatch between the piston and probe signals. Piston and probe waves are then orthogonally polarized by means of two polarization controllers, combined in a first polarization beam splitter (PBS), and injected into a 13-km-long dispersion compensating fiber (DCF from OFS). The DCF fiber spool is characterized by a normal chromatic dispersion D = –130 ps/nm/km at 1550 nm (β_2 = 166 ps^2/km), an attenuation parameter α = 0.4 dB/km and a nonlinear Kerr coefficient γ' = 5.5 $W^{-1}.km^{-1}$. At the output of the system, the piston pulse beam and the CW probe are polarization demultiplexed using a second PBS and characterized both in the temporal and spectral domains by means of two high-speed photodetectors from U2T connected to a dual-channel 70-GHz electrical sampling oscilloscope (Agilent DCA 86118A) and an optical spectrum analyzer (OSA Yokogawa AQ6370), respectively. Note that before temporal detection, a tunable optical bandpass filter from Exfo may be inserted in such a way to carry out a spectral-temporal analysis (see Fig. 5d). Finally, the entire experimental platform was automatically controlled from a single computer, which enables us to accumulate up to 150 measurements in a very short time scale, providing perfect stability whilst mapping the entire shock dynamics.

APPENDIX C: Details of the oscillatory pattern of the shock fan

As can be observed in the experimental recording of the ballistic shock wave depicted in Fig. 5b of the manuscript, the DSW is characterized by a wide-open temporal gap surrounded by two strongly modulated wave trains that link the high humps to the CW boundaries. The periods and temporal positions of these oscillations can be fully explained by the dispersion-induced spectro-temporal mapping of the shock phenomenon. Indeed, since the oscillations can be understood to arise from the interference between the CW components and highly chirped edges of the probe beam, the temporal oscillations of the shock can be approximated as $1 + 2\cos\left(t^2/2\beta_2 L\right)$. In order to demonstrate this point, we have reported in Fig. 7 the evolution of the pattern frequencies and corresponding temporal positions of these oscillations along the shock fan. The experimental results corresponding to

the maxima of the red curve in Fig. 5b of the article (here in green stars) match very well with these predictions (orange solid line). Moreover, we can also notice the good agreement obtained through numerical simulations of the shock (circles) based on Eqs.(1) as well as the corresponding spectro-temporal evolution of the pump (in yellow squares), thus confirming the genuine dispersive mapping of these vectorial interactions.

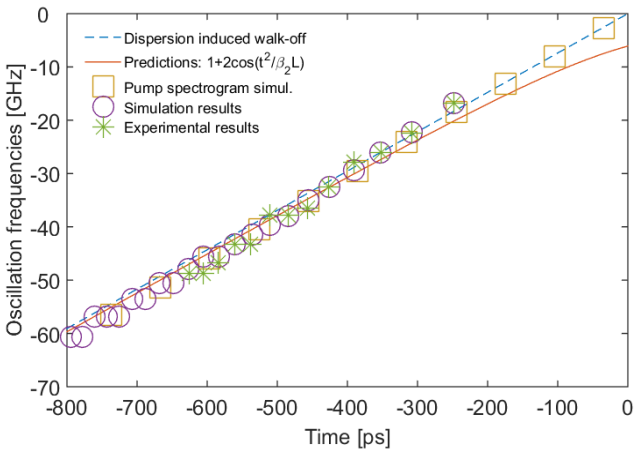

Figure 7. Temporal mapping of the shock oscillation frequencies. The experimental results extracted from Fig. 5b of the main manuscript (green stars) are compared with numerical simulations (in purple circles) and walk-off induced by chromatic dispersion mapping (blue dashed line). Theoretical predictions are included with an orange solid line while the pump spectrogram, obtained from numerical simulations, is also highlighted by means of yellow squares.

References

1. T. A. Coleman, K. R. Knupp, and D. Herzmann, "The spectacular undular bore in Iowa on 2 October 2007," Mon. Wea. Rev. **137**, 495 (2009).
2. H. Chanson, *Tidal bores Aegir, Eagre, Mascaret, Proroca: Theory and Observations* (World Scientific, 2012).
3. R. H. Clarke, R. K. Smith, and D. G. Reid, "The Morning Glory of the gulf of Carpentaria: An atmospheric undular bore," Mon. Wea. Rev. **109**, 1726 (1981).
4. S. Hodges and A. Carverhill, "Quasi-mean reversion in an efficient stock market; the characterization of economic equilibria which support Black–Scholes option pricing," Econom. J. **103**, 395 (1993).
5. G. B. Whitham, *Linear and Nonlinear Waves* (Wiley, New York, 1974).
6. G. A. El and M. A. Hoefer, "Dispersive shock waves and modulation theory," Physica D **333**, 11-65 (2016).
7. E. Rolley, C. Guthmann, and M. S. Pettersen, "The hydraulic jump and ripples in liquid helium," Physica B **394**, 46-55 (2007).
8. M. A. Hoefer, M. J. Ablowitz, I. Coddington, E. A. Cornell, P. Engels, and V. Schweikhard, "Dispersive and classical shock waves in Bose-Einstein condensates and gas dynamics," Phys. Rev. A **74**, 023623 (2006).
9. J. E. Rothenberg and D. Grischkowsky, "Observation of the formation of an optical intensity shock and wave-breaking in the nonlinear propagation of pulses in optical fibers," Phys. Rev. Lett. **62**, 531-534 (1989).
10. W. Wan, S. Jia, and J. W. Fleischer, "Dispersive superfluid-like shock waves in nonlinear optics," Nat Phys **3**, 46-51 (2007).
11. S. Jia, W. Wan, and J. W. Fleischer, "Forward four-wave mixing with defocusing nonlinearity," Opt. Lett. **32**, 1668 (2007).
12. N. Ghofraniha, S. Gentilini, V. Folli, E. DelRe, and C. Conti, "Shock Waves in Disordered Media," Phys. Rev. Lett **109**, 243902 (2012).
13. B. Wetzel, D. Bongiovanni, M. Kues, Y. Hu, Z. Chen, S. Trillo, J. M. Dudley, S. Wabnitz, and R. Morandotti, "Experimental Generation of Riemann Waves in Optics: A Route to Shock Wave Control," Phys. Rev. Lett **117**, 073902 (2016).
14. J. Fatome, C. Finot, G. Millot, A. Armaroli, and S. Trillo, "Observation of Optical Undular Bores in Multiple Four-Wave Mixing," Phys. Rev. X **4**, 021022 (2014).
15. B. Varlot, S. Wabnitz, J. Fatome, G. Millot, and C. Finot, "Experimental generation of optical flaticon pulses," Opt. Lett. **38**, 3899-3902 (2013).
16. G. Xu, A. Mussot, A. Kudlinski, S. Trillo, F. Copie, and M. Conforti, "Shock wave generation triggered by a weak background in optical fibers," Opt. Lett **41**, 2656-2659 (2016).
17. G. Xu, M. Conforti, A. Kudlinski, A. Mussot, and S. Trillo, "Dispersive dam-break flow of a photon fluid," Phys. Rev. Lett. **118**, 254101 (2017).
18. S. Trillo and A. Valiani, "Hydrodynamic instability of multiple four-wave mixing," Opt. Lett **35**, 3967-3969 (2010).
19. Y. Kodama and S. Wabnitz, "Analytical theory of guiding-center nonreturn-to-zero and return-to-zero signal transmission in normally dispersive nonlinear optical fibers," Opt. Lett. **20**, 2291-2293 (1995).
20. S. Wabnitz, C. Finot, J. Fatome, and G. Millot, "Shallow water rogue wavetrains in nonlinear optical fibers," Phys. Lett. A **377**, 932-939 (2013).
21. A. Parriaux, M. Conforti, A. Bendahmane, J. Fatome, C. Finot, S. Trillo, N. Picqué, and G. Millot, "Spectral broadening of picosecond pulses forming dispersive shock waves in optical fibers," Opt. Lett. **42**, 3044-3047 (2017).
22. A. M. Kamchatnov, G. A., and R. A. Kraenkel, "Dissipationless shock waves in Bose–Einstein condensates with repulsive interaction between atoms," Phys. Rev. A **69**, 063605 (2004).
23. Z. Dutton, M. Budde, C. Slowe, and L. V. Hau, "Observation of Quantum Shock Waves Created with Ultra- Compressed Slow Light Pulses in a Bose-Einstein Condensate," Science **293**, 663 (2001).

24. R. J. Taylor, D. R. Baker, and H. Ikezi, "Observation of Collisionless Electrostatic Shocks," Physical Review Letters **24**, 206-209 (1970).
25. J. A. Joseph, J. E. Thomas, M. Kulkarni, and A. G. Abanov, "Observation of Shock Waves in a Strongly Interacting Fermi Gas," Physical Review Letters **106**, 150401 (2011).
26. C. Barsi, W. Wan, S. Jia, and J. W. Fleischer, "Spatially Dispersive Shock Waves," in *nonlinear photonics and novel optical phenomena* (Springer, 2012).
27. R. Stoughton, "Measurements of small caliber ballistic shock waves in air," J. Acoust. Soc. Am. **102**, 781-786 (1997).
28. M. A. Hoefer, M. J. Ablowitz, and P. Engels, "Piston Dispersive Shock Wave Problem," Physical Review Letters **100**, 084504 (2008).
29. M. E. Mossman, M. A. Hoefer, K. Julien, P. G. Kevrekidis, and P. Engels, "Dissipative shock waves generated by a quantum-mechanical piston," Nature Communications **9**, 4665 (2018).
30. G. A. El, A. Gammal, and A. M. Kamchatnov, "Generation of oblique dark solitons in supersonic flow of Bose-Einstein condensate past an obstacle," Nuclear Physics A **790**, 771c-775c (2007).
31. G. A. El, A. M. Kamchatnov, V. V. Khodorovskii, E. S. Annibale, and A. Gammal, "Two-dimensional supersonic nonlinear Schrödinger flow past an extended obstacle," Physical Review E **80**, 046317 (2009).
32. G. A. El and A. Kamchatnov, "Spatial dispersive shock waves generated in supersonic flow of Bose–Einstein condensate past slender body," Phys. Lett. A **350**, 192-196 (2006).
33. G. P. Agrawal, *Nonlinear Fiber Optics, Fourth Edition* (Academic Press, San Francisco, CA, 2006).
34. P. K. A. Wai, C. R. Menyuk, and H. H. Chen, "Stability of solitons in randomly varying birefringent fibers," Opt. Lett. **16**, 1231-1233 (1991).
35. D. Marcuse, C. R. Menyuk, and P. K. A. Wai, "Application of the Manakov-PMD equation to studies of signal propagation in optical fibers with randomly varying birefringence," J. Lightw. Technol. **15**, 1735-1746 (1997).
36. D. Anderson, M. Desaix, M. Lisak, and M. L. Quiroga-Teixeiro, "Wave-breaking in nonlinear optical fibers," J. Opt. Soc. Am. B **9**, 1358-1361 (1992).
37. C. Finot, B. Kibler, L. Provost, and S. Wabnitz, "Beneficial impact of wave-breaking on coherent continuum formation in normally dispersive nonlinear fibers," J. Opt. Soc. Am. B **25**, 1938-1948 (2008).
38. A. Zeytunyan, G. Yesayan, L. Mouradian, P. Kockaert, P. Emplit, F. Louradour, and A. Barthélémy, "Nonlinear-dispersive similariton of passive fiber," J. Europ. Opt. Soc. Rap. Public. **4**, 09009 (2009).
39. D. Castelló-Lurbe, P. Andrés, and E. Silvestre, "Dispersion-to-spectrum mapping in nonlinear fibers based on optical wave-breaking," Opt. Express **21**, 28550-28558 (2013).
40. A. Mahjoubfar, D. V. Churkin, S. Barland, N. Broderick, S. K. Turitsyn, and B. Jalali, "Time stretch and its applications," Nat. Photon. **11**, 341 (2017).
41. S. O. Iakushev, O. V. Shulika, and I. A. Sukhoivanov, "Passive nonlinear reshaping towards parabolic pulses in the steady-state regime in optical fibers," Opt. Commun. **285**, 4493-4499 (2012).
42. M. N. Islam, L. F. Mollenauer, R. H. Stolen, J. R. Simpson, and H. T. Shang, "Cross-phase modulation in optical fibers," Opt. Lett. **12**, 625-627 (1987).
43. E. B. Treacy, "Measurement and Interpretation of Dynamic Spectrograms of Picosecond Light Pulses," Journal of Applied Physics **42**, 3848-3858 (1971).
44. S. Linden, H. Giessen, and J. Kruhl, "XFROG - A new method for amplitude and phase characterization of weak ultrashort pulses," Phys. Stat. Sol. **206**, 119-124 (1998).
45. A. Niedzwiecki and H. S. Ribner, "Subjective loudness of N-wave sonic booms," J. Acoust. Soc. Am. **64**, 1617-1621 (1978).
46. T. Congy, A. Kamchatnov, and N. Pavloff, "Dispersive hydrodynamics of nonlinear polarization waves in two-component Bose-Einstein condensates," SciPost Physics **1**, 006 (2016).
47. C. Finot, "Dispersion managed self-similar parabolic pulses," Journal of Optics A: Pure and Applied Optics **10**, 085101 (2008).